Fabrication of $Bi_2O_2CO_3$/g-C_3N_4 heterojunctions for efficiently photocatalytic NO in air removal: *In-situ* self-sacrificial synthesis, characterizations and mechanistic study

Zhenyu Wang [a,b], Yu Huang [b,c,*], Wingkei Ho [d], Junji Cao [a,b,c,**], Zhenxing Shen [e], Shun Cheng Lee [f]

[a] School of Human Settlements and Civil Engineering, Xi'an Jiaotong University, Xi'an 710049, China
[b] Key Lab of Aerosol Chemistry & Physics, Institute of Earth Environment, Chinese Academy of Sciences, Xi'an 710061, China
[c] State Key Lab of Loess and Quaternary Geology (SKLLQG), Institute of Earth Environment, Chinese Academy of Sciences, Xi'an 710061, China
[d] Department of Science and Environmental Studies, The Hong Kong Institute of Education, Hong Kong, China
[e] Department of Environmental Science and Engineering, Xi'an Jiaotong University, Xi'an 710049, China
[f] Department of Civil and Environmental Engineering, The Hong Kong Polytechnic University, Hung Hom, Hong Kong, China

ARTICLE INFO

ABSTRACT

Layer-structured $Bi_2O_2CO_3$/g-C_3N_4 heterojunction photocatalysts were successfully prepared *via* one-pot hydrothermal method for the first time, in which graphitic carbon nitride (g-C_3N_4) served as the self-sacrificial reagent to supply carbonate anions simultaneously. Our results showed that the *in situ* fabricated $Bi_2O_2CO_3$/g-C_3N_4 heterojunction exhibited superior visible-light-driven photocatalytic activity for NO photocatalytic oxidation, which can be ascribed to the morphology and structure modulation during the sacrificial synthesis processes. Heterojunctions formation pathways underlying temperature- and time-dependent structure evolution were discussed in detail. The sample fabricated at 160 °C for 12 h (BOC-CN-160) showed high stability and durability, and the highest NO removal rate which is up to 34.8% under visible light irradiation. Results from photocurrent tests and electrochemical impedance spectroscopy (EIS) demonstrated that the BOC-CN-160 sample presents much more effective interface charge separation efficiency, which can contribute to its remarkably improved photocatalytic performance. Reactive radicals during the photocatalysis processes were identified by electron spin resonance (ESR) study. Combined with the quantification of reaction intermediates, the photocatalytic degradation mechanism of NO over $Bi_2O_2CO_3$/g-C_3N_4 heterojunction photocatalyst was proposed. The novel approach developed in this study may be further extended to synthesize a series of novel and highly efficient g-C_3N_4-based carbonate heterojunction photocatalysts for visible light-harvesting and energy conversion applications.

© 2016 Elsevier B.V. All rights reserved.

1. Introduction

With the rapid urbanization and development of China, the concentration levels of $PM_{2.5}$ ($PM \leq 2.5\,\mu m$ in aerodynamic diameter) in major megacities remains remarkably higher than that of the National Ambient Air Quality Standard [1–3]. Previous studies showed that secondary organic aerosols (SOAs), which are formed *via* the photochemical reactions with NO_x ($NO + NO_2 = NO_x$) and volatile organic compounds (VOCs) as precursors, contributed significantly to the mass concentrations of $PM_{2.5}$ [4–6]. As an alternative to conventional approaches (selective catalytic reduction and wet scrubbing, *etc.*) with high cost adopted for high-concentration NO_x treatment [7], semiconductor photocatalysis has gained considerable attention not only because of its potential value in addressing the worldwide energy shortage, but also because of its eco-friendly merit and high efficiency for the remediation of NO_x at part-per-billion (ppb) levels [8–13].

A suitable band gap structure of semiconductor photocatalyst is essential for light harvesting and photo-induced carriers separating and migrating, which facilitates the occurring of redox reaction thermodynamically [14]. Single semiconductor cannot fulfill the

* Corresponding author at: Key Lab of Aerosol Chemistry & Physics, Institute of Earth Environment, Chinese Academy of Sciences, Xi'an 710061, China.
** Corresponding author at: School of Human Settlements and Civil Engineering, Xi'an Jiaotong University, Xi'an 710049, China.
E-mail addresses: huangyu@ieecas.cn (Y. Huang), cao@loess.llqg.ac.cn (J. Cao).

above harsh terms simultaneously. Hence, numerous strategies, such as element doping [15], noble deposition [16], and surface modification [17], have been developed to improve the photocatalytic activities of catalysts in the past decade. Recently, exploring semiconductor/semiconductor photocatalytic heterojunctions that mainly contain type-I/II/III heterojunctions, p/n–n heterojunctions, Z-scheme system, and homojunction for photocatalytic performance improvement has been paid more and more attention [18,19]. In contrast to single semiconductors, heterostructure composites not only effectively restrain the recombination of photoinduced e$^-$–h$^+$ pairs, but also markedly endow nanohybrids with enhanced properties or unique features through their synergistic catalytic effects [20].

$Bi_2O_2CO_3$, consisted of $[Bi_2O_2]^{2+}$ slabs interleaved between two slabs of CO_3^{2-}, possesses an Aurivillius-layered structure that exerts a low mammalian toxicity and displays a wide band gap (3.1–3.5 eV) [21,22] (Fig. S1). The compound has been used in medical treatment for a long time and as a photocatalyst in recent years [21,23]. However, $Bi_2O_2CO_3$ photocatalysts can only absorb UV light (less than 5% of the solar light) and exhibit a poor charge carriers separation ability, which seriously restrict the photocatalytic performance of this type photocatalysts. Therefore, various methods have been recently employed to overcome the intrinsic limitations of $Bi_2O_2CO_3$ photocatalysts, mainly including element doping (N, C, CO_3^{2-}, Bi, Ag-doping $Bi_2O_2CO_3$) [24–28], and heterojunction fabrication ($Bi_2O_2CO_3/BiVO_3$, $Bi_2O_2CO_3/BiOX$ (X = Cl, Br, and I), $Bi_2O_2CO_3/\alpha$-Bi_2O_3, $Bi_2O_2CO_3/Ag_2O$, and $Bi_2S_3/Bi_2O_3/Bi_2O_2CO_3$) [22,29–35]. Among these approaches, the fabrication of heterojunctions was preferred by many researchers because it can maximize the advantages of each component to offset their individual weaknesses. Graphitic carbon nitride (g-C_3N_4) is a metal-free, visible-light, covalent binary CN polymer organic semiconductor photocatalyst with a 2D layered structure which is analogous to that of graphite [36,37]. This material has attracted considerable interest due to its unique physicochemical property and electronic band structure [38], which has been potentially applied in fields that are related to solar energy conversion [39,40], environmental remediation [41,42], bioimaging [43], and material science [44,45].

Considering the unique features of $Bi_2O_2CO_3$ and g-C_3N_4, a rational strategy is to combine the merits of each component to fabricate heterojunction nanocomposites with intrinsic layer-structure. Various methodologies have been adopted to construct $Bi_2O_2CO_3$/g-C_3N_4 heterojunction in order to extend the optical absorption and improve the quantum yield of $Bi_2O_2CO_3$. For example, Zhang et al. [46] prepared $(BiO)_2CO_3$/g-C_3N_4 heterojunction photocatalysts by the deposition of $(BiO)_2CO_3$ onto the surface of g-C_3N_4 for the efficient capture of atmospheric CO_2 at room temperature. Xiong et al. [47] prepared flower-like g-C_3N_4/$Bi_2O_2CO_3$ microspheres with a high adsorption ability via chemical precipitation method. Zhang et al. [48] designed novel g-C_3N_4/$Bi_2O_2CO_3$ nanojunction photocatalysts through self-assembly and chemical precipitation. However, all of these mentioned synthesis strategies for $Bi_2O_2CO_3$/g-C_3N_4 heterojunction fabrication require the addition of extra carbonate sources (such as CO_2 or Na_2CO_3), and normally require two main steps. The pristine component is prepared firstly and then deposited with another component to construct heterojunctions. These procedures are difficult to construct heterojunctions with uniform structures because of compatibility issues among different components. Therefore, constructing heterojunction structures with homogeneous distribution of components remains challenging.

In this study, layer-structured $Bi_2O_2CO_3$/g-C_3N_4 heterojunction photocatalysts were successfully prepared with a one-pot hydrothermal strategy via self-sacrificing a part of g-C_3N_4 to supply CO_3^{2-} for $Bi_2O_2CO_3$ formation for the first time. The pre-

pared $Bi_2O_2CO_3$/g-C_3N_4 heterojunctions exhibit a considerably higher photocatalytic activity than any single phase on NO in air degradation under visible light irradiation. The mechanisms underlying structural evolution, NO removal, and photocatalytic activity enhancement are discussed through the combination of experimental results and theoretical analysis. This novel synthesis strategy can be probably extended to synthesize a series of highly efficient, visible light-driven g-C_3N_4-based carbonate heterojunction photocatalysts.

2. Experimental

2.1. Synthesis of $Bi_2O_2CO_3$/g-C_3N_4 heterojunction samples

All chemicals were used without further purification. $Bi_2O_2CO_3$/g-C_3N_4 composites (BOC/CN for short) were synthesized using a hydrothermal approach. In a typical process, 2.0 g of $Bi(NO_3)_3 \cdot 5H_2O$ was dispersed in 40 mL of HNO_3 (0.02 M) and stirred for 30 min. Then, 0.9 g of g-C_3N_4 was added to the above solution. After 45 min of ultrasonic treatment, 0.625 M NaOH was added to adjust the pH to 8.0–8.5. The mixture was transferred into a 100 mL Teflon-lined autoclave and heated for 12 h at 140 °C, 160 °C, or 180 °C or heated at 160 °C for 4, 8, or 12 h. After cooling down to room temperature naturally, the products were collected by filtration, washed thoroughly with deionized water and absolute ethanol for three times, dried at 60 °C for 12 h, and then denoted as BOC-CN-140, BOC-CN-160, and BOC-CN-180, and BOC-CN-160-4, BOC-CN-160-8, and BOC-CN-160-12, respectively. For comparison, Na_2CO_3 was used instead of g-C_3N_4 to synthesize $Bi_2O_2CO_3$ in the same manner at 160 °C, and g-C_3N_4 used in this experiment was prepared according to the previously reported method [49] (Supplementary information).

2.2. Characterization methods

The crystal phase was analyzed via X-ray diffraction (XRD) with Cu Kα radiation at a scan rate of 0.05°2θ/s (λ = 1.5406 Å, 40 kV, 40 mA, PANalytical X' Pert PRO X-ray diffractometer). Samples were embedded in KBr pellets and then subjected to Fourier-transform infrared spectroscopy (FT-IR) on an FT-IR absorption spectrometer (Magna-IR 750, Nicolet, USA). X-ray photoelectron spectroscopy (XPS) was conducted using an X-ray photoelectron spectrometer (Thermo ESCALAB 250, USA). All binding energies were calibrated to the C 1 s peak at 284.7 eV of the surface adventitious carbon. Elemental analyses were carried out on a Elementar Vario EL instrument (Vario EL III, German, detection limit: 0.015%, standard deviation: ≤0.1% abs) with He purging for 20 s prior to testing. Scanning electron microscopy (SEM, JEOL JSM-6490, Japan) was used to characterize the morphology and elemental distribution maps of the obtained products. Transmission electron microscopy (TEM) was performed using a JEOL JEM-2100HR CM-120 (Japan) transmission electron microscope. Moreover, a nitrogen adsorption apparatus (ASAP 2020, USA) was used to obtain the nitrogen adsorption–desorption isotherms of the samples that were degassed at 150 °C prior to analysis. A Varian Cary 100 Scan UV–vis system equipped with a labsphere diffuse reflectance accessory was used to obtain the reflectance spectra of the catalysts over a range of 200–800 nm. Labsphere USRS-99-010 was employed as a reflectance standard. The intermediate and final products, nitrate and nitrite ions, were extracted by immersing the powders (about 0.05 g) into 6 mL deionized water and measured by using a Dionex-600 Ion Chromatograph (IC, Dionex Inc., Sunny-vale, CA, USA) after the photocatalytic activity test equipped with an IonPac AS14A column. The mobile phase was composed of a mixture of 1.8 mM Na_2CO_3 and 1.7 mM $NaHCO_3$ at a flow rate of 1.20 mL/min, the vol-

ume of samples was 20 μL. The detection limits for NO_2^- and NO_3^- are 0.0050 μg mL^{-1} and 0.0256 μg mL^{-1}. Samples for electron spin-resonance spectroscopy (ESR, ER200-SRC, Bruker, Germany) were prepared by mixing 0.05 g of the as-prepared photocatalyst in a 25 mM 5,5′-dimethyl-1-pirroline-*N*-oxide (DMPO) solution with a 50 mL aqueous dispersion for DMPO-•OH or a 50 mL alcohol dispersion for DMPO-•O_2^- under irradiation with 420 nm visible light.

2.3. Photoelectrochemical measurements

Photoelectrochemical properties of the as-prepared samples were evaluated using a Parstat 4000 electrochemical workstation (USA) in a conventional three-electrode cell, with a platinum plate and an Ag/AgCl electrode as the counter and reference electrodes, respectively. The photocurrent-time curves were measured at 0.2 V versus Ag/AgCl in 0.5 mol/L Na_2SO_3 at ambient temperature under a 300 W Xe lamp (microsolar 300, Perfectlight, China) with 420 nm. Electrochemical impedance spectroscopy (EIS) was measured at a frequency range of 0.1 Hz to 100 kHz with an 5 mV voltage amplitude under an open-circuit voltage in a 1 mmol/L $K_3Fe(CN)_6$ and $K_4Fe(CN)_6$ solution.

2.4. Photocatalytic activity test

The photocatalytic activity of the as-prepared samples were investigated in terms of NO removal at ppb levels in a continuous flow reactor system (Fig. S2) at ambient temperature. The rectangular reactor, which was fabricated from stainless steel and covered with quartz glass, possessed a volume capacity of 4.5 L (30 cm × 15 cm × 10 cm). A 300 W commercial Xe arc lamp (microsolar 300, Perfectlight, China) was vertically placed outside the reactor. UV light in the light beam was removed by adopting a UV cutoff filter (420 nm). The photocatalyst (0.1 g) was coated onto one dish (10.0 cm in diameter), which was subsequently pre-treated at 60 °C to remove water in the suspension. NO gas was supplied by a compressed gas cylinder at a concentration of 48 ppm (N_2 balance) in accordance with the standard of the National Institute of Standards and Technology. The initial NO concentration was diluted to 400 ppb by an air stream supplied by a zero-air generator (Model 1001, Sabio Instruments LLC, Georgetown, TX, USA), and the flow rate was controlled at 3 L/min. The desired relative humidity level of NO flow was controlled at 70% by passing zero air streams through a humidification chamber. The lamp was turned on when the adsorption-desorption equilibrium was achieved. The concentration of NO was continuously measured using a chemiluminescence NO analyzer (Model 42c, Thermo Environmental Instruments Inc., Franklin, MA, USA). This apparatus was used to monitor NO and NO_2 concentrations at a sampling rate of 0.6 L/min. The removal ratio (η) of NO was calculated as η (%) = (1−C/C$_0$) × 100, where C and C$_0$ are the concentrations of NO in the outlet and feeding streams, respectively.

3. Results and discussion

3.1. Phase structure and chemical compositions

Fig. 1a shows the XRD patterns of the as-prepared BOC, BOC-CN-160, and CN samples. Apparently, all diffraction peaks for BOC can be readily indexed to pure tetragonal $Bi_2O_2CO_3$ (a = 3.865 Å, b = 3.865 Å, c = 13.675 Å, JCPDS no. 41-1488) without other diffraction peaks being detected [50]. Two distinct diffraction peaks located at 2θ = 13.1° and 27.6° in g-C_3N_4 are attributed to the (100) crystal plane of tri-s-triazine units and the (002) crystal plane of interlayer stacking of aromatic segments, respectively [38,51]. The typical diffraction peaks of BOC and CN can also be observed in the

BOC-CN-160 composite, demonstrating that $Bi_2O_2CO_3$/g-C_3N_4 heterojunction has been successfully constructed by self-sacrificing parts of g-C_3N_4 as CO_3^{2-} provider. It is interesting to find that the (002), (004), and (006) peaks corresponding to the {001} facets of BOC exhibited overwhelmingly higher relative intensity than those of the heterojunction. Moreover, the intensity of (002) peaks belonging to CN decreases significantly because of the self-sacrifice reaction. It could be deduced that the BOC {001} facet growing in situ from the CN {002} facet leads to the simultaneous decrease in intensity of the (002) peaks in CN and the (002), (004), and (006) peaks in BOC. These results imply that the coupling of CN-BOC heterojunctions probably occurs between the BOC {001} and CN {002} facets. In addition, the phase structure of the obtained products evolved obviously as revealed by the results from temperature-dependent experiments. As shown in Fig. S3, the signal for $Bi_2O_2CO_3$ phase cannot be detected, and the main diffraction peaks for BOC-CN-140 can be indexed to tetragonal bismuth oxide nitrate hydroxide ($Bi_2O_2(OH)NO_3$, Fig. S4 presents the schematic crystal structure of $Bi_2O_2(OH)NO_3$), indicating that anions (NO_3^- and OH^-) cannot overcome the kinetic barrier to exchange with CO_3^{2-} under this hydrothermal condition, and $[Bi_2O_2]^{2+}$ covering the CN surface leads to the weak intensity of the CN feature peaks in BOC-CN-140. After hydrothermal treatment at 180 °C, a well-crystallized tetragonal $Bi_2O_2CO_3$ is formed, and no obvious CN peaks can be observed, which implies g-C_3N_4 may be decomposed almost completely in aqueous solution reaction under this condition.

The FT-IR spectra of the BOC, BOC-CN-160, and CN are shown in Fig. 1b. The following typical bands of pure BOC are observed: an absorption band at 845 cm^{-1}, which is assigned to the out-of-plane bending mode of CO_3^{2-}, and an absorption band at 1390 and 1467 cm^{-1}, which is assigned to the antisymmetric vibration mode of CO_3^{2-} [52]. For pure CN, the intensive bands in the 1200–1700 cm^{-1} region indicate the stretching vibration of the heptazine heterocyclic ring (C_6N_7) units. The peak at 807 cm^{-1} is associated with the breathing mode of the heptazine ring system, whereas the absorption band at 890 cm^{-1} is assigned to the deformation mode of N—H. In addition, the broad band at 3400–3600 cm^{-1} is due to physically adsorbed H_2O [42,53]. The BOC-CN-140 sample shows the characteristic absorption bands of both $Bi_2O_2(OH)NO_3$ [54] and g-C_3N_4 (Fig. S5). The BOC-CN-160 sample shows the characteristic absorption bands of both BOC and g-C_3N_4, thereby confirming the co-presence of BOC and g-C_3N_4 components. The results of XRD and FT-IR indicate that $Bi_2O_2CO_3$/g-C_3N_4 heterojunction can be successfully fabricated by this *in situ* method using g-C_3N_4 as the sacrificial agent. In BOC-CN-180 sample (Fig. S5), the characteristic absorption bands of BOC were quite stronger than CN, which means little parts of undecomposed CN existed in BOC-CN-180.

The surface composition and coupling mode among atoms in the CN-BOC-160 heterojunctions are further analyzed by XPS. The surveyed spectra in Fig. 2a implies the presence of Bi, O, C, and N in the prepared nanocomposite sample without other element signals being detected. The two peaks at 164.2 and 158.9 eV in BOC are associated with Bi $4f_{5/2}$ and Bi $4f_{7/2}$ of Bi^{3+} [55,56], respectively (Fig. 2b). The distinct binding energy drifts observed in BOC-CN-160 can be attributed to the change in inner electron density caused by the formation of the BOC-CN heterojunction. In the C 1s region (Fig. 2c), the sharp peak around 284.6 eV is attributed to the pure graphitic species in the CN matrix [51], and the peak at 284.7 eV in BOC is assigned to adventitious carbon species from XPS measurement. The C 1s peak around 288.0 eV in the BOC-CN-160 sample can be assigned to the overlapping peaks of carbonate ion in BOC and the sp^2-hybridized carbon in trizine rings (N—C=N) [51,57]. In the N 1s region (Fig. 2d), the main N 1s peak around the binding energy of 398.2 eV can be assigned to the sp^2 hybridized aromatic N
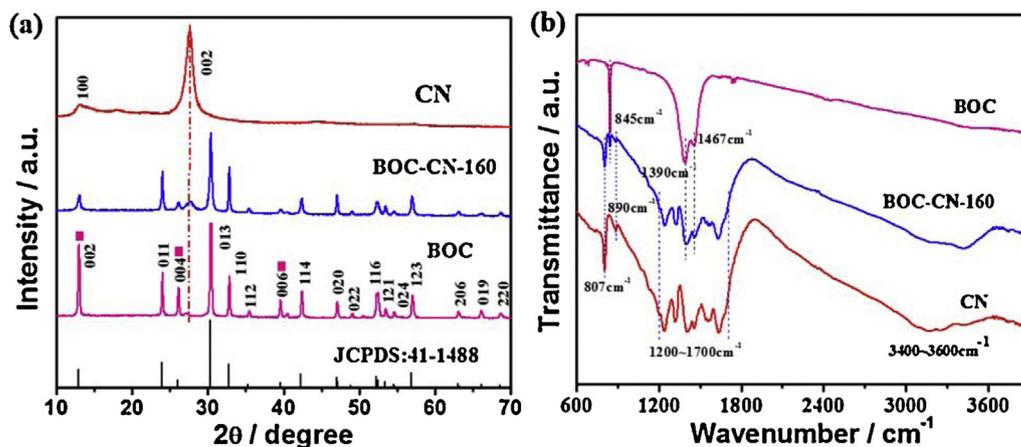
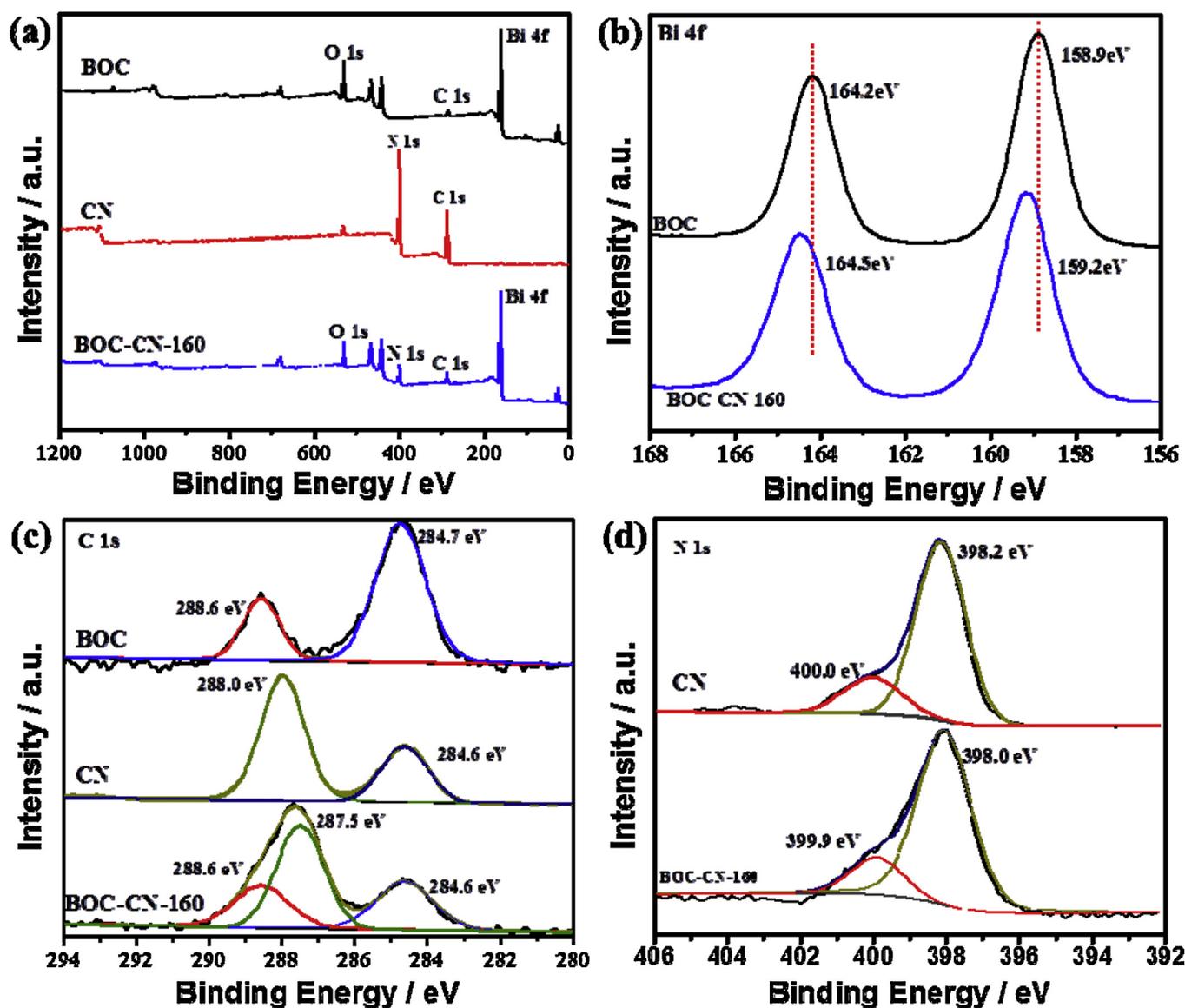**Fig. 1.** XRD patterns (a) and FT-IR spectra (b) of pristine BOC, BOC-CN-160, and CN.

Fig. 2. Survey XPS spectra (a) and high-resolution XPS spectra of Bi 4f (b), C 1s (c), and N 1s (d) of the as-prepared samples.

bonded to carbon atoms (C=N—C), and the weak peak at 400.0 eV is attributed to the tertiary nitrogen N–(C)$_3$ groups or H—N–(C)$_2$ [58] in both CN and BOC-CN-160 samples.

In order to investigate the constituent content of BOC-CN-160 sample quantificationally, the C and N elements were chosen to estimate the Bi$_2$O$_2$CO$_3$ and C$_3$N$_4$ contents in heterojunction by ele-

mental analysis method and the results were listed in Table S1. From the results, the C contents in BOC, BOC-CN-160, and CN are 2.347%, 14.964% and 36.835%, respectively. The N contents in BOC-CN-160, and CN are 22.940%, and 61.977%. Therefore, the mass contents of $Bi_2O_2CO_3$ and $g-C_3N_4$ in the CN-BOC-160 composites are estimated to be 56.994% and 36.566%, respectively.

3.2. Morphological structure and texture property

The morphologies of the representative samples are examined by using SEM and TEM analysis. As displayed in Fig. 3a, the BOC products are composed of large-scale, round pill-like nanoplates. A close-up view of the nanoplates in Fig. 3b indicates that the nanoplates are ca. 100–250 nm thick. The quadrate $Bi_2O_2CO_3$ nanoplatelets anchor on the bulk $g-C_3N_4$ surface to be assembled into $Bi_2O_2CO_3/g-C_3N_4$ nanocomposites, as shown in Fig. 3c. The $Bi_2O_2CO_3$ nanoplates are ca. 100 nm to 1.5 μm in length and 40–80 nm in thickness (Fig. 3d). The elemental mapping images of the same low region (Figs. 3e–h) indicate that Bi, O, N, and C are homogeneously distributed on the obtained heterojunction and that the extra C on the background is attributed to the signal from conductive sellotape.
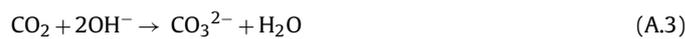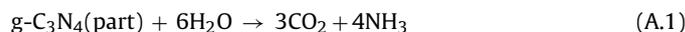
Transmission electron microscopy (TEM) is used to investigate the morphological structures of the samples, as shown in Fig. 4. As displayed in Fig. 4a and consistent with SEM results (Fig. 3a), the large-scale, irregular pill-like nanoplates of the BOC sample are further verified and observed. The low-magnification TEM image (Fig. 4b) shows that individual CN consists of a typical layer structure with different sizes and irregular shapes. The square $Bi_2O_2CO_3$ nanosheets attach on the $g-C_3N_4$ surface to assemble $Bi_2O_2CO_3/g-C_3N_4$ nanocomposites, as shown in Fig. 4c. The HRTEM image of the BOC square nanosheet in the BOC-CN-160 sample reveals a lattice spacing of approximately 0.275 nm, which can be ascribed to the (110) plane of tetragonal BOC (JCPDS 41–1488), as shown in Fig. 4d. The single-crystalline nature of BOC in the BOC-CN-160 sample is confirmed by a selected-area electron diffraction (SAED) pattern, which is assigned to the [001] zone-axis diffraction spots of tetragonal BOC [23] (Fig. 4e). Based on these results, it can be assumed that the {001} facet of BOC in the BOC-CN-160 sample is exposed. Moreover, combining with the results of SEM and TEM, it is interesting to find that the dimension and thickness of the layers of $Bi_2O_2CO_3$ (Fig. 3d) and C_3N_4 (Fig. 4c) in the BOC-CN-160 sample are reduced and become much thinner than those of $Bi_2O_2CO_3$ (Fig. 3b) synthesized through the conventional method with the addition of extra carbonate precursors and those of original $g-C_3N_4$ (Fig. 4b), which can be ascribed to the occurrence of the $g-C_3N_4$ self-sacrifice effect during the synthesis processes. The HR-TEM image of $g-C_3N_4$ is shown in Fig. S6a, and the similar morphology in BOC-CN-160 heterojunction and meanwhile the (110) plane of BOC (lattice spacing of 0.274 nm) can be observed in Fig. S6b, suggesting the intimate interfacial contact between BOC and $g-C_3N_4$.

The nitrogen adsorption-desorption isotherms are displayed in Fig. S7. The results show all samples are of type IV (BDDT classification) [59], suggesting the presence of mesopores. The specific surface areas are 4, 27, and 10 m^2/g for BOC, BOC-CN-160, and CN, respectively. The large specific surface area for BOC-CN-160 was associated with the morphological transformation, parts of bulk $g-C_3N_4$ with low surface area self-sacrifice and quadrate $Bi_2O_2CO_3$ nanoplatelets with high surface area formation, which can be evidenced by SEM and TEM.

3.3. Formation mechanism

According to the phase structure and morphologies analysis, a schematic illustration of the fabrication of $Bi_2O_2CO_3/g-C_3N_4$ heterojunctions using $g-C_3N_4$ as the self-sacrificial reagent to sup-

ply carbonate anions is proposed (Scheme 1). $Bi_2O_2(OH)NO_3$ and $Bi_2O_2CO_3$ are composed of $[Bi_2O_2]^{2+}$ layers sandwiched between two slabs of anions or groups, facilitating the potential phase transformation from $Bi_2O_2(OH)NO_3$ to $Bi_2O_2CO_3$ in theory [58]. The heterojunction fabrication strategy in this study involves the formation of a $[Bi_2O_2]^{2+}$ cage structure template and the process of anion exchange. As shown in Scheme 1, CO_3^{2-} does not exchange with NO_3^- and OH^- in $Bi_2O_2(OH)NO_3$ to form $Bi_2O_2CO_3$ under 140 °C, which means a high hydrothermal energy is required to overcome the kinetic barrier for anion exchange because of the higher stability of $Bi_2O_2CO_3$ than that of $Bi_2O_2(OH)NO_3$. Moreover, $g-C_3N_4$ suffers from decomposition in liquid water at the proper temperature, similar to mesoporous silica SBA-15, and generates NH_4^+ and CO_3^{2-} during hydrothermal treatment [60,61]. However, few people can take advantage of this property for composite fabrication (Process 1). When the temperature is increased to 160 °C, the tetragonal $Bi_2O_2CO_3$ is obtained (Process 2), as evidenced by the XRD results (Fig. S3a). These assumptions were also supported by the results from time-dependent hydrothermal experiments to investigate the growth and ripening processes of $Bi_2O_2CO_3/g-C_3N_4$ heterojunctions at 160 °C (Fig. S3b). Fig. S3b shows that the $Bi_2O_2(OH)NO_3$ phase is gradually transformed into $Bi_2O_2CO_3$ as the reaction time is prolonged from 4 h to 12 h at 160 °C (Process 3). Therefore, combining the experimental results regarding to the evolution of morphology and structure and the schematic description is Scheme 1, the formation process of the heterostructured $Bi_2O_2CO_3/g-C_3N_4$ composite in this study can be described by the following equations (Eqs. (A.1)–(A.6)):

$$g-C_3N_4(part) + 6H_2O \rightarrow 3CO_2 + 4NH_3 \tag{A.1}$$

$$NH_3 + H_2O \rightarrow NH_4^+ + OH^- \tag{A.2}$$

$$CO_2 + 2OH^- \rightarrow CO_3^{2-} + H_2O \tag{A.3}$$

$$2Bi^{3+} + NO_3^- + 5OH^- \rightarrow Bi_2O_2(OH)NO_3 + 2H_2O \tag{A.4}$$

$$Bi_2O_2(OH)NO_3 + CO_3^{2-} \rightarrow Bi_2O_2CO_3 + NO_3^- + OH^- \tag{A.5}$$

$$Bi_2O_2CO_3 + g-C_3N_4(others) \rightarrow Bi_2O_2CO_3/g-C_3N_4 heterojunction \tag{A.6}$$

3.4. Band gap structure of $Bi_2O_2CO_3/g-C_3N_4$ heterojunctions

In general, the photocatalytic activity of the photocatalyst is closely related to its band structure. The UV–vis DRS was used to investigate the optical properties of the obtained samples, as shown in Fig. 5. For the pure BOC sample, the basal absorption edge occurs at a wavelength shorter than 360 nm, whereas the absorption intensity of $g-C_3N_4$ shows absorption edges at 480 nm (Fig. 5a). In comparison to BOC, the absorption band edge of BOC-CN-160 exhibits an apparent red shift with the introduction of CN. This shift is ascribed to the interaction between CN and BOC semiconductors in heterojunctions. The band energies (E_g), which are estimated from the intercept of tangents to the plots of $(\alpha h\nu)^{1/2}$ versus photo energy [7] (Fig. 5b), are 2.43 and 3.28 eV for CN and BOC, respectively. The VB and CB potentials of a semiconductor material can be estimated using the following empirical equations [34]:

$$E_{VB} = \chi - E^e + 0.5E_g$$

$$E_{CB} = E_{VB} - E_g,$$

where E_{VB}/E_{CB} is the valence/conduction band edge potential, and χ is the Sanderson electronegativity of the semiconductor, which is defined as the geometric average of the absolute electronegativity of the constituent atoms. E^e is the energy of free electrons on the hydrogen scale (about 4.5 eV versus NHE), and E_g is the band gap energy of the semiconductor. The χ-values for BOC and $g-C_3N_4$ are approximately 6.54 and 4.73 eV [34,62], respectively. On the basis
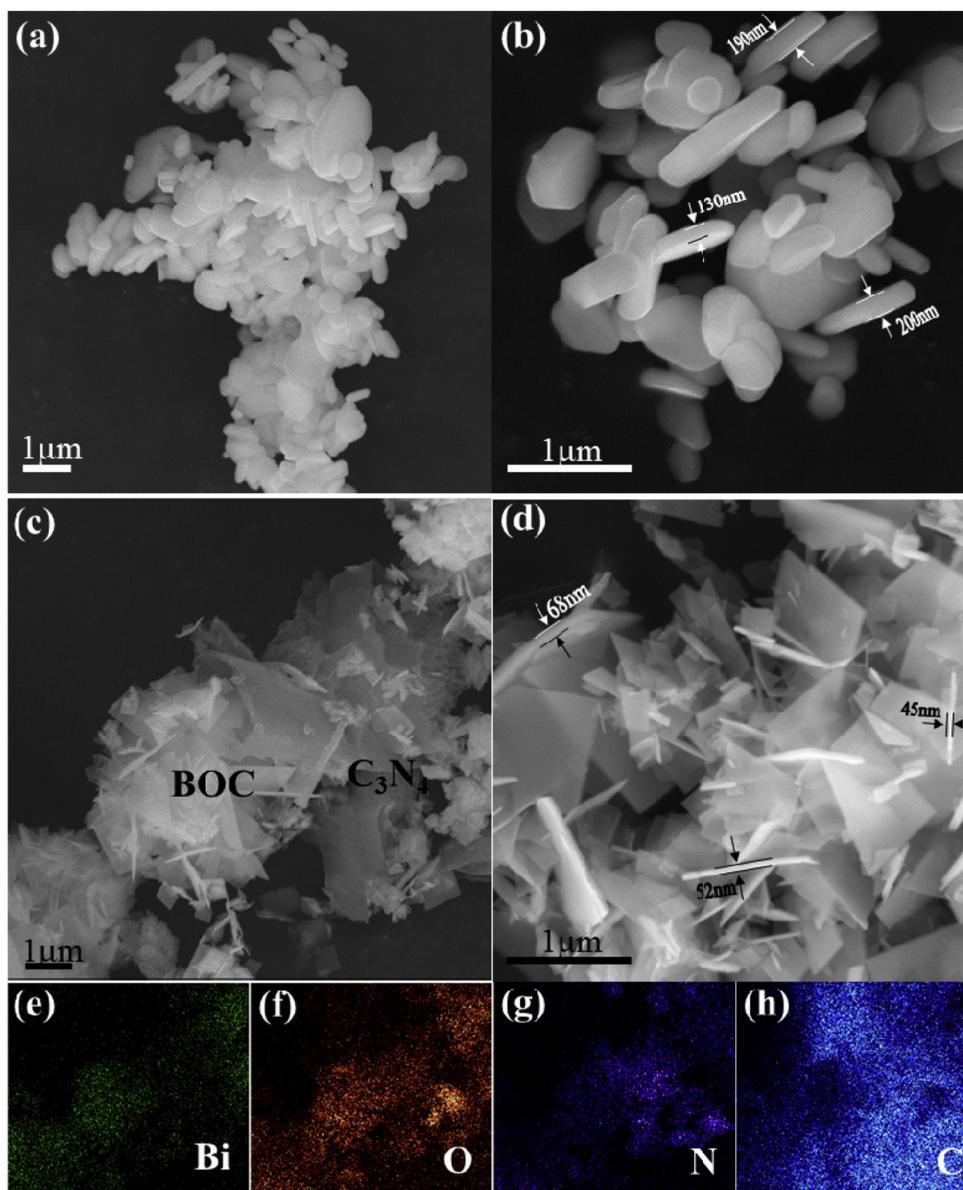
Fig. 3. SEM images of BOC at low (a) and high magnifications (b), BOC-CN-160 at low (c) and high magnifications (d), and elemental distribution maps of the same low region indicating the spatial distribution of Bi (green, e), O (red, f), N (purple, g), and C (blue, h). (For interpretation of the references to colour in this figure legend, the reader is referred to the web version of this article.)

Table 1
Calculated CB, VB position, band gap energy, S_{BET}, NO removal ratios, and reaction rate constant for BOC, BOC-CN-160, and CN.

Samples	Calculated CB position (V)	Calculated VB position (V)	Band gap E_g (eV)	S_{BET} (m^2/g)	NO removal ratio η (%)	Reaction rate constant k (min^{-1})
BOC	0.40	3.68	3.28	4	5.4	0.005
BOC-CN-160	–	–	–	27	34.8	0.077
CN	−0.99	1.44	2.43	10	21.6	0.050

of the above data, the top of the VB and the bottom of the CB of BOC are calculated to be 3.68 and 0.40 V, and the VB and CB of CN are estimated to be 1.44 and −0.99 V, respectively. The energy band structures of BOC and CN are listed in Table 1.

3.5. Photocatalytic activity and stability

The as-prepared BOC, BOC-CN-X (X = 140, 160, and 180), and CN samples were employed in the photocatalytic removal of NO under visible light irradiation in a continuous reactor to demon-strate their potential capability in air purification. NO cannot be photolyzed under light irradiation without the aid of photocataly-sis [25,63]. Figure 6a shows the variation of NO concentration over the as-prepared photocatalysts (C/C$_0$%) with irradiation time. The NO concentrations decreased rapidly in the first 5 min because of the photocatalytic reaction and finally reach a stable value in all the cases. The removal ratios of NO by BOC, BOC-CN-180, BOC-CN-160, BOC-CN-140, and CN are 5.4%, 26.1%, 34.8%, 23.3%, and 21.6% after 30 min of visible light irradiation, respectively. In order to make a clearly quantitative comparison, we used the Langmuir-
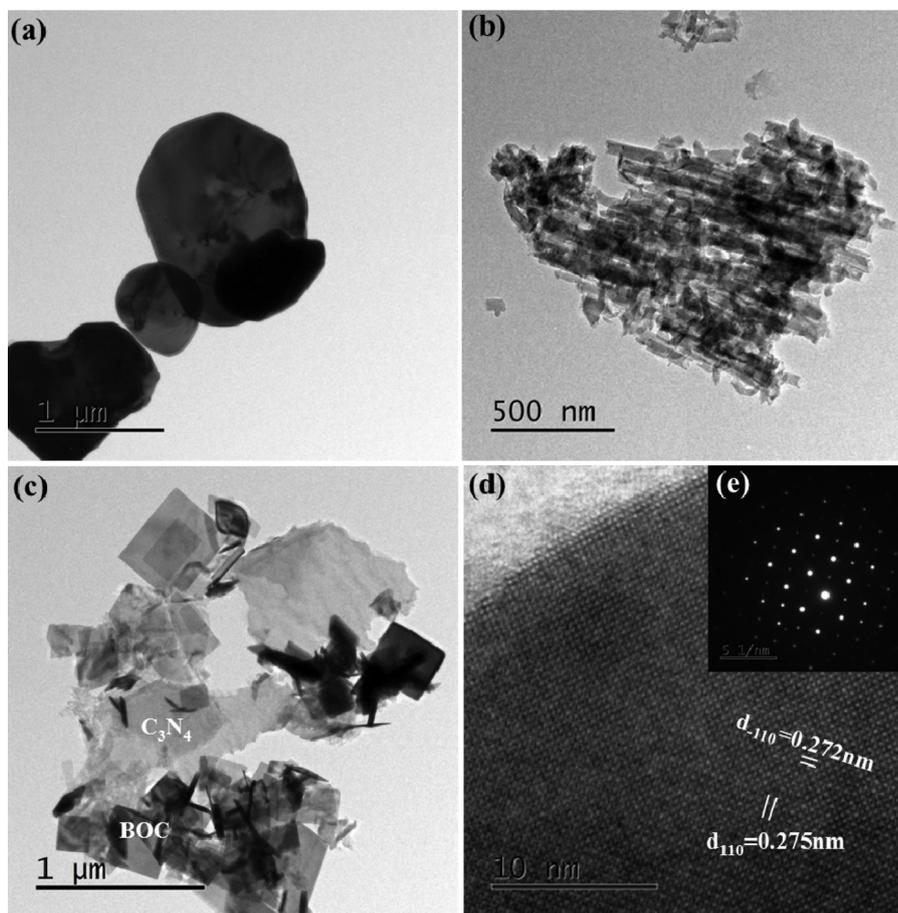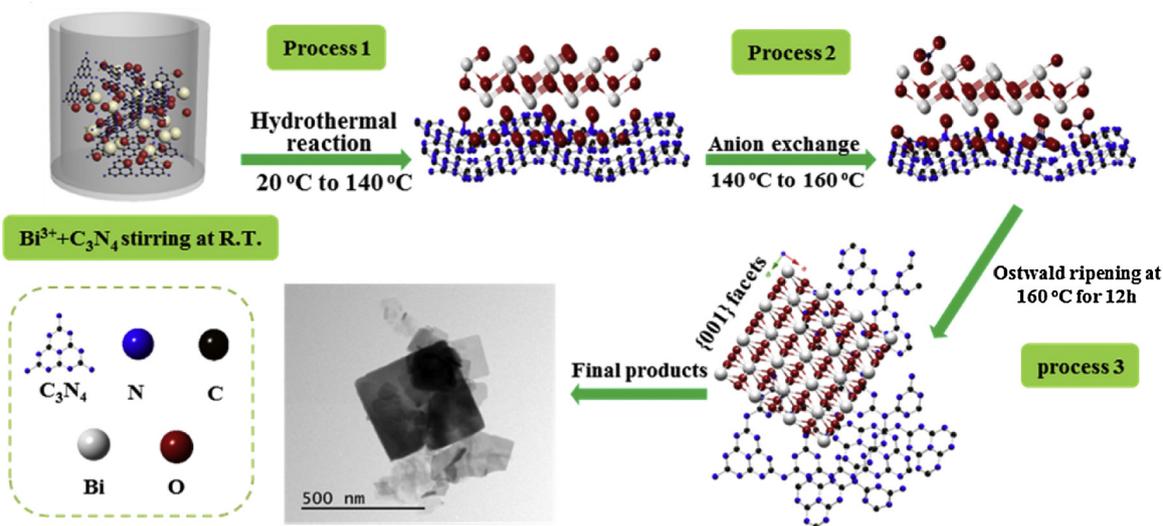
Fig. 4. Low-magnification TEM image of pristine BOC (a), CN (b), and BOC-CN-160 (c); HRTEM (d) and SAED images (e) of BOC square nanoplatelet of BOC-CN-160.

Scheme 1. Schematic illustration of the synthesis process of $Bi_2O_2CO_3$/g-C_3N_4 heterojunctions *via* g-C_3N_4 self-sacrifice to achieve anion exchange strategy.

Hinshelwood model in reaction kinetics to describe the rates of NO photodegradation [64]. According to previous study [65], the initial photocatalytic degradation of NO was approximately simulated to follow mass-transfer-controlled pseudo-first-order rate reaction. (Details about Langmuir-Hinshelwood model and apparent reaction rate constant k calculations are given in the ESI†). The apparent reaction rate constant k of BOC-CN-160 ($0.077 \, min^{-1}$) is 15.4, 2.5, 1.6, and 1.5 times higher than those of BOC ($0.005 \, min^{-1}$),

BOC-CN-180 ($0.031 \, min^{-1}$), BOC-CN-140 ($0.047 \, min^{-1}$), and CN ($0.050 \, min^{-1}$), respectively (Fig. S8). Evidently, the BOC-CN-160 heterojunction exhibits the highest NO removal ratio and k among all the as-prepared samples. During the process of NO photocatalytic oxidation, NO_2, as a reaction intermediate, can form and hinder for the photocatalyst application because of its toxicity. Thus, the by-product of NO_2 is monitored online and selectivity is calculated (Fig. S9a and details about NO_2 selectivity are given in
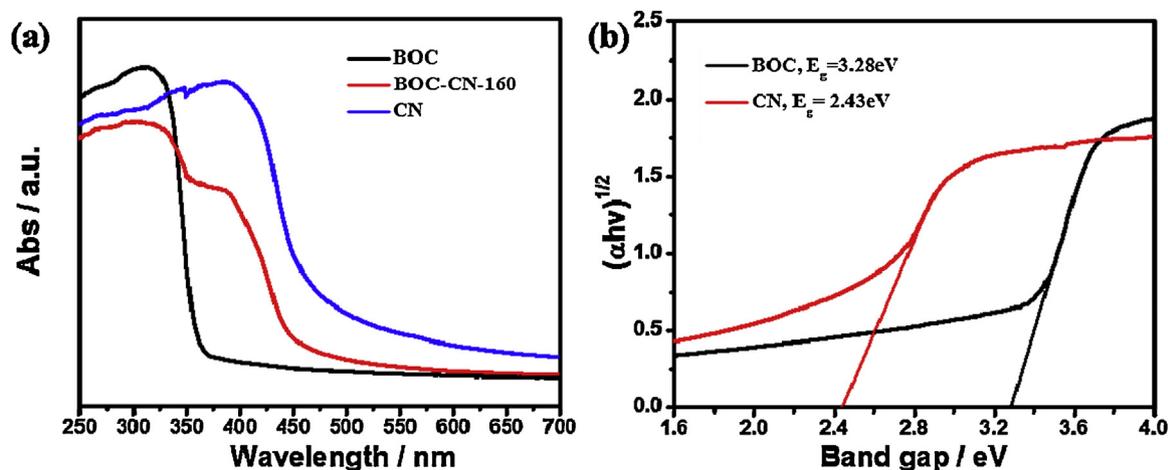
Fig. 5. UV–vis diffuse reflectance spectra (a) and plots of $(\alpha h\nu)^{1/2}$ versus the photo energy (b) of the as-synthesized BOC, BOC-CN, and CN nanocomposites.
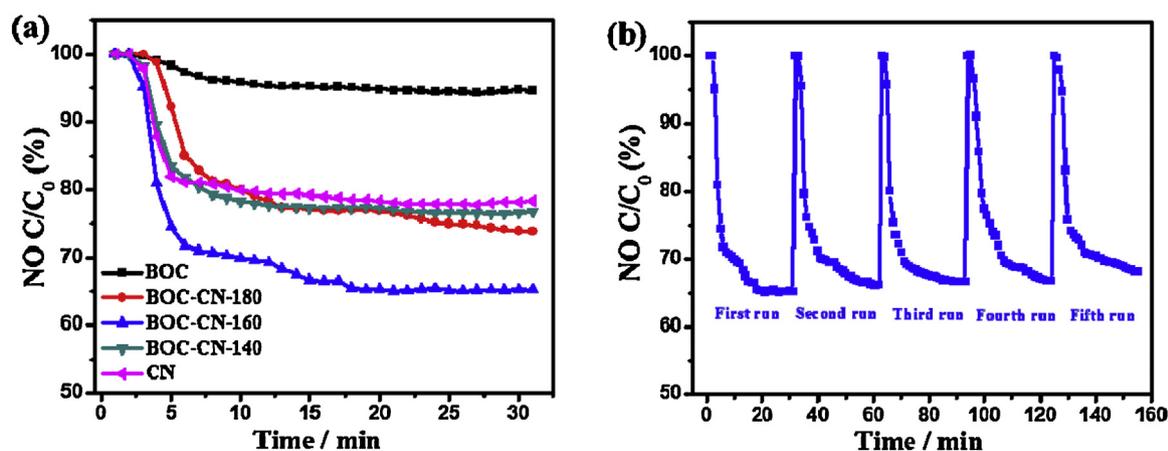

Fig. 6. (a) Visible light photocatalytic activities of the BOC, BOC-CN-X (X = 140, 160, 180), and CN samples for NO removal in air; (b) cycling runs for the photocatalytic degradation of NO over BOC-CN-160 under visible light irradiation.

the ESI†). The results show BOC-CN-160 displays the lowest conversion ratio of NO to NO_2 than others (Fig. S9b). Above results imply that the BOC-CN-160 heterojunction is more advantageous under realistic conditions because of outstanding NO degradation and NO_2 inhibition. The removal of NO can be attributed to the reaction between NO and photogenerated radicals, producing the final products of HNO_2 and HNO_3. In order to investigate the reaction pathways for the photocatalytic oxidation of NO_x, the accumulated NO_2^- and NO_3^- on the surface of BOC-CN-160 after single run reaction were extracted by deionized water and measured by ion chromatography (IC) method. It was found that the amounts of NO_3^- accumulated on BOC-CN-160 surface were 7.956 μmol, but no NO_2^- was detected, which indicated that the oxidation of NO to NO_3^- was the major conversion process. It was found that the amount of NO degradation products as determined by IC analysis was lower than the total amount of removed NO (11.81 μmol) according to nitrogen mass balance. This can be attributed to the release of NO_2^- or NO_3^- into humidified air (RH 70%), or the generation of some new species undetectable by NO_x analyzer or IC, as Ai et al. reported [65]. Reproducibility and stability are important to photocatalysts for potential applications. To examine photocatalytic stability, cycling runs for the photocatalytic removal of NO with the BOC-CN-160 sample were performed under the same conditions. Fig. 6b illustrates the relationship between NO removal ratio and cycling times. After undergoing five repeated runs, the NO removal ratio remains high, indicating that BOC-CN-160 is sta-

ble in activity and can be used repeatedly. The used BOC-CN-160 sample is collected and analyzed by XRD and FT-IR (Fig. S10). Evidently, the crystal structure of used BOC-CN-160 sample is identical to that of the fresh sample, implying that the sample is stable and durable in structure.

3.6. Mechanism for NO removal and photocatalytic activity enhancement

To identify the formation of reactive radicals of the BOC-CN-160 sample accounting for NO removal, ESR spectroscopy with DMPO spin-trapping adducts was performed to allow the detection of superoxide radicals (DMPO-$\bullet O_2^-$) in methanol and hydroxyl radicals (DMPO-$\bullet OH$) in aqueous state. As shown in Fig. 7a, four apparent signals were generated, which can be attributed to $\bullet O_2^-$ with BOC-CN-160 *via* the reduction of O_2 with photo-generated electrons in methanol under visible light irradiation for 5 min. Meanwhile, no $\bullet O_2^-$ signal was observed in the dark under otherwise identical conditions. In Fig. 7b, DMPO-$\bullet OH$ adduct signals that are weaker than DMPO-$\bullet O_2^-$ signals were also detected in the system containing the $Bi_2O_2CO_3/g\text{-}C_3N_4$ composite. The E_{VB} of g-C_3N_4 (1.44 V) is lower than the standard redox potential of $H_2O/\bullet OH$ (2.37 V) but is higher than that of HNO_3/NO (0.94 V), indicating that the photogenerated holes of g-C_3N_4 could not oxidize H_2O to active species $\bullet OH$ but may oxidize NO (Eq. (B.2)) [66]. This result confirms that $\bullet O_2^-$ is the dominant active species in NO_x oxidation. The $\bullet OH$

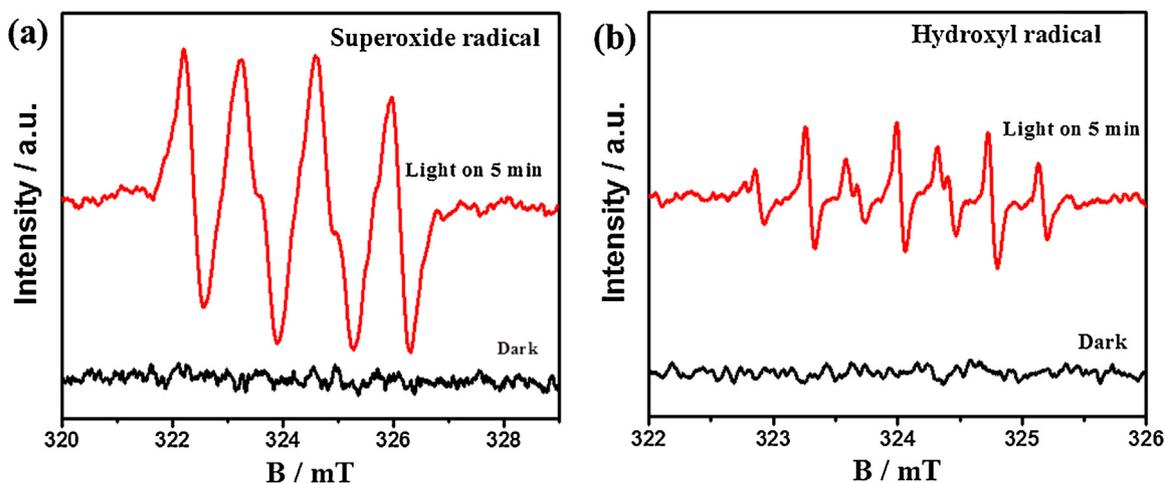**Fig. 7.** DMPO spin-trapping ESR spectra of BOC-CN-160 in methanol dispersion for DMPO-•O$_2^-$ (a) and in aqueous dispersion for DMPO-•OH (b).
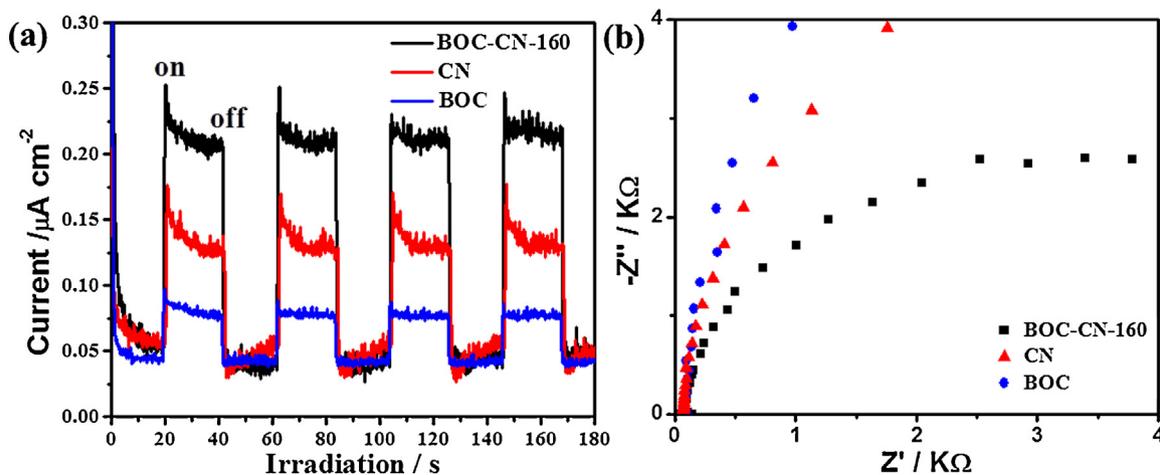

Fig. 8. Photocurrent transient (a) and Nyquist plots (b) for BOC-CN-160, CN, and BOC electrodes under visible light irradiation ($\lambda > 420$ nm).

radicals perform a minor function and should be generated *via* the −•O$_2^-$ → •OH route (Eq. (B.4)) [42].

As revealed in Fig. 8a, transient photocurrent responses with good reproducibility were observed for the BOC-CN-160, CN, and BOC electrodes under visible light. These responses are directly correlated with the recombination efficiency of the photogenerated carriers. As forecasted, the weak photocurrent density of pure BOC can be detected because of the large energy gap, and decent photocurrent response singles of CN were detected. In contrast to both BOC and CN, the BOC-CN-160 nanohybrid exhibits a remarkably enhanced photocurrent density. This result confirms the more efficient charge separation of the BOC-CN-160 nanohybrid than BOC and CN because pure BOC acts as an electron acceptor in the heterojunction structure than that in the single phases. In addition, EIS measurements were carried out to further investigate the charge transfer resistance and separation efficiency of the charge carriers. Fig. 8b shows that BOC-CN-160 presents a smaller arc radius than the other samples under visible light irradiation ($\lambda > 420$ nm). This result validates the high efficiency of charge transfer and separation of BOC-CN-160 [67]. In other words, the BOC-CN-160 nanohybrid exhibits lower resistance than the other samples and can facilitate the separation and immigration of photogenerated carriers under visible light irradiation.

Based on the above characterizations and analysis, the *in situ* fabricated Bi$_2$O$_2$CO$_3$/g-C$_3$N$_4$ heterojunction exhibited superior visible-light-driven photocatalytic activity for NO photocatalytic

oxidation, which can be ascribed to the morphology and structure modulation during the sacrificial synthesis processes. The BOC-CN-160 heterojunction with the layered hierarchical structure of square BOC nanosheets show the highest BET surface area (27 m^2/g), which was favorable for reaction site increase, initial NO adsorption, and intermediates diffusion. More importantly, the synergistic effects of BOC-CN-160, including well-matched band structures, intimate interfacial contact, and effective separation of the photoinduced carriers, can be of great advantage to NO photocatalytic oxidation. The related mechanisms for NO removal and photocatalytic activity enhancement over Bi$_2$O$_2$CO$_3$/g-C$_3$N$_4$ heterojunction are proposed accordingly as illustrated in Fig. 9. g-C$_3$N$_4$ can be excited by visible light and generate photo-induced electrons and holes (Eq. (B.1)), but BOC cannot be subjected to identical conditions because of a wide band gap. The CB edge potential of g-C$_3$N$_4$ (−0.99 V) is more negative than that of Bi$_2$O$_2$CO$_3$ (0.40 V), allowing the excited electron on the g-C$_3$N$_4$ surface to transfer easily to Bi$_2$O$_2$CO$_3$ *via* the well-matched heterojunction under visible light irradiation. Thus, the photo-generated electrons and holes can be separated effectively, and the recombination of photogenerated charge would be sufficiently inhibited. Then, the photoelectrons electrons are trapped by O$_2$ in the surrounding air to form reactive •O$_2^-$ (Eq. (B.3)). NO$_x$ reacts with the photo-generated −•O$_2^-$ and •OH radicals, and then NO$_3^-$ ions are produced (Eqs. (B.5)–(B.7)). The reaction processes of photocatalytic NO removal

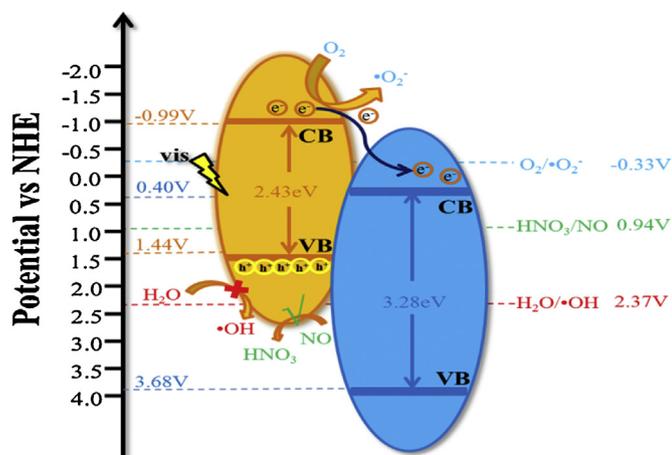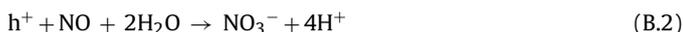**Fig. 9.** Proposed photocatalytic mechanism for enhancing photocatalytic activity over $Bi_2O_2CO_3/g-C_3N_4$ heterojunctions under visible light irradiation.

by the $Bi_2O_2CO_3/g-C_3N_4$ heterojunction are described as the following (Eqs. (B.1)–(B.7)):

$$g-C_3N_4 + h\nu \rightarrow e^- + h^+ \tag{B.1}$$

$$h^+ + NO + 2H_2O \rightarrow NO_3^- + 4H^+ \tag{B.2}$$

$$e^- + O_2 \rightarrow {}^\bullet O_2^- \tag{B.3}$$

$${}^\bullet O_2^- + 2H^+ + 2e^- \rightarrow {}^\bullet OH + OH^- \tag{B.4}$$

$$NO_x + {}^\bullet O_2^- \rightarrow NO_3^- \tag{B.5}$$

$$2{}^\bullet OH + NO \rightarrow NO_2 + H_2O \tag{B.6}$$

$$NO_2 + {}^\bullet OH \rightarrow NO_3^- + H^+ \tag{B.7}$$

4. Conclusion

Heterostructured $Bi_2O_2CO_3/g-C_3N_4$ nanocomposites with partial self-sacrificed $g-C_3N_4$ as the precursor of carbonate anion were successfully prepared by one-pot hydrothermal treatment for the first time. Compared with pristine $Bi_2O_2CO_3$ and $g-C_3N_4$, the BOC-CN-160 heterojunction sample exhibits dramatically enhanced visible light photocatalytic activity for the degradation of NO with the highest apparent reaction rate, attributing to favorable texture property and synergistic effects. In addition, the electrons, which are excited from $g-C_3N_4$ by irradiating BOC-CN-160 heterojunction under visible light, are trapped by O_2 in the surrounding air to form reactive ${}^\bullet O_2^-$ radicals, which were identified as the main active species in the photocatalytic reaction by ESR. The reaction mechanisms of photocatalytic NO removal by the $Bi_2O_2CO_3/g-C_3N_4$ heterojunction are discussed in detail. The *in situ* self-sacrificial synthesis strategy developed in this study may supply a new route for the fabrication of highly efficient C_3N_4-based carbonate heterostructures for environmental and energy applications in the future.

Notes

Acknowledgements

Appendix A. Supplementary data

Supplementary data associated with this article can be found, in the online version, at http://dx.doi.org/10.1016/j.apcatb.2016.06.027.

References

[1] R.-J. Huang, Y. Zhang, C. Bozzetti, K.-F. Ho, J.-J. Cao, Y. Han, K.R. Daellenbach, J.G. Slowik, S.M. Platt, F. Canonaco, Nature 514 (2014) 218–222.
[2] S. Guo, M. Hu, M.L. Zamora, J. Peng, D. Shang, J. Zheng, Z. Du, Z. Wu, M. Shao, L. Zeng, Proc. Natl. Acad. Sci. U. S. A. 111 (2014) 17373–17378.
[3] Y. Sun, G. Zhuang, A. Tang, Y. Wang, Z. An, Environ. Sci. Technol. 40 (2006) 3148–3155.
[4] L.S. Brickus, J.N. Cardoso, F.R. de Aquino Neto, Environ. Sci. Technol. 32 (1998) 3485–3490.
[5] R. Pathak, W. Wu, T. Wang, Atmos. Chem. Phys. 9 (2009) 1711–1722.
[6] N. Ng, P. Chhabra, A. Chan, J. Surratt, J. Kroll, A. Kwan, D. McCabe, P. Wennberg, A. Sorooshian, S. Murphy, Atmos. Chem. Phys. 7 (2007) 5159–5174.
[7] F. Dong, Z. Wang, Y. Li, W.-K. Ho, S. Lee, Environ. Sci. Technol. 48 (2014) 10345–10353.
[8] Q. Liu, Y. Zhou, J. Kou, X. Chen, Z. Tian, J. Gao, S. Yan, Z. Zou, J. Am. Chem. Soc. 132 (2010) 14385–14387.
[9] D. Spasiano, R. Marotta, S. Malato, P. Fernandez-Ibañez, I. Di Somma, Appl. Catal. B: Environ. 170 (2015) 90–123.
[10] R. Portela, R. Tessinari, S. Suarez, S. Rasmussen, M. Hernandez-Alonso, M. Canela, P. Avila, B. Sanchez, Environ. Sci. Technol. 46 (2012) 5040–5048.
[11] Y. Huang, W. Ho, S. Lee, L. Zhang, G. Li, J.C. Yu, Langmuir 24 (2008) 3510–3516.
[12] D. Zhang, M. Wen, S. Zhang, P. Liu, W. Zhu, G. Li, H. Li, Appl. Catal. B: Environ. 147 (2014) 610–616.
[13] Y. Huang, Y. Gao, Q. Zhang, J.-j. Cao, R.-j. Huang, W. Ho, S.C. Lee, Appl. Catal. A: Gen. 515 (2016) 170–178.
[14] S. Chen, L.-W. Wang, Chem. Mater. 24 (2012) 3659–3666.
[15] Y. Huang, W. Ho, Z. Ai, X. Song, L. Zhang, S. Lee, Appl. Catal. B: Environ. 89 (2009) 398–405.
[16] Q. Zhang, Y. Huang, L. Xu, J.-j. Cao, W. Ho, S.C. Lee, ACS Appl. Mater. Interfaces (2016).
[17] Y. Li, Y. Wang, Y. Huang, J. Cao, W. Ho, S. Lee, C. Fan, RSC Adv. 5 (2015) 99712–99721.
[18] H. Wang, L. Zhang, Z. Chen, J. Hu, S. Li, Z. Wang, J. Liu, X. Wang, Chem. Soc. Rev. 43 (2014) 5234–5244.
[19] H. Li, Y. Zhou, W. Tu, J. Ye, Z. Zou, Adv. Funct. Mater. 25 (2015) 998–1013.
[20] J. Shi, Chem. Rev. 113 (2012) 2139–2181.
[21] M.H.S.R. Chen, J. Yang, F. Deng, C.M. Che, H.Z. Sun, Chem. Commun. (2006) 2265–2267.
[22] P. Madhusudan, J. Ran, J. Zhang, J. Yu, G. Liu, Appl. Catal. B: Environ. 110 (2011) 286–295.
[23] H. Huang, J. Wang, F. Dong, Y. Guo, N. Tian, Y. Zhang, T. Zhang, Cryst. Growth Des. 15 (2015) 534–537.
[24] Y. Zhou, Z. Zhao, F. Wang, K. Cao, D.E. Doronkin, F. Dong, J.-D. Grunwaldt, J. Hazard. Mater. 307 (2016) 163–172.
[25] T. Xiong, H. Huang, Y. Sun, F. Dong, J. Mater. Chem. A 3 (2015) 6118–6127.
[26] H. Huang, X. Li, J. Wang, F. Dong, P.K. Chu, T. Zhang, Y. Zhang, ACS Catal. 5 (2015) 4094–4103.
[27] F. Dong, Q. Li, Y. Sun, W.-K. Ho, ACS Catal. 4 (2014) 4341–4350.
[28] S. Peng, L. Li, H. Tan, Y. Wu, R. Cai, H. Yu, X. Huang, P. Zhu, S. Ramakrishna, M. Srinivasan, J. Mater. Chem. A 1 (2013) 7630–7638.
[29] L. Yu, X. Zhang, G. Li, Y. Cao, S. Yu, D. Li, Appl. Catal. B: Environ. (2016).
[30] J. Cao, X. Li, H. Lin, B. Xu, S. Chen, Q. Guan, Appl. Surf. Sci. 266 (2013) 294–299.
[31] L. Chen, S.-F. Yin, S.-L. Luo, R. Huang, Q. Zhang, T. Hong, P.C. Au, Ind. Eng. Chem. Res. 51 (2012) 6760–6768.
[32] R. Hu, X. Xiao, S. Tu, X. Zuo, J. Nan, Appl. Catal. B: Environ. 163 (2015) 510–519.
[33] Y. Huang, W. Wang, Q. Zhang, J.-j. Cao, R.-j. Huang, W. Ho, S.C. Lee, Sci. Rep. 6 (2016) 23435.
[34] N. Liang, M. Wang, L. Jin, S. Huang, W. Chen, M. Xu, Q. He, J. Zai, N. Fang, X. Qian, ACS Appl. Mater. Interfaces 6 (2014) 11698–11705.
[35] Y. Huang, W. Fan, B. Long, H. Li, F. Zhao, Z. Liu, Y. Tong, H. Ji, Appl. Catal. B: Environ. 185 (2016) 68–76.
[36] Y. Wang, X. Wang, M. Antonietti, Angew. Chem. Int. Ed. 51 (2012) 68–89.
[37] J. Zhang, Y. Chen, X. Wang, Energy Environ. Sci. 8 (2015) 3092–3108.
[38] X. Wang, K. Maeda, A. Thomas, K. Takanabe, G. Xin, J.M. Carlsson, K. Domen, M. Antonietti, Nat. Mater. 8 (2009) 76–80.
[39] S. Cao, J. Yu, J. Phys. Chem. Lett. 5 (2014) 2101–2107.
[40] G. Zhang, M. Zhang, X. Ye, X. Qiu, S. Lin, X. Wang, Adv. Mater. 26 (2014) 805–809.
[41] T. Sano, S. Tsutsui, K. Koike, T. Hirakawa, Y. Teramoto, N. Negishi, K. Takeuchi, J. Mater. Chem. A 1 (2013) 6489–6496.
[42] Z. Wang, W. Guan, Y. Sun, F. Dong, Y. Zhou, W.-K. Ho, Nanoscale 7 (2015) 2471–2479.
[43] X. Zhang, X. Xie, H. Wang, J. Zhang, B. Pan, Y. Xie, J. Am. Chem. Soc. 135 (2012) 18–21.
[44] Y. Zheng, J. Liu, J. Liang, M. Jaroniec, S.Z. Qiao, Energy Environ. Sci. 5 (2012) 6717–6731.

[45] G. Li, Z. Lian, W. Wang, D. Zhang, H. Li, Nano Energy 19 (2016) 446–454.
[46] W. Zhang, Y. Sun, F. Dong, W. Zhang, S. Duan, Q. Zhang, Dalton Trans. 43 (2014) 12026–12036.
[47] M. Xiong, L. Chen, Q. Yuan, J. He, S.-L. Luo, C.-T. Au, S.-F. Yin, Dalton Trans. 43 (2014) 8331–8337.
[48] Q. Zhang, H. Wang, S. Hu, G. Lu, J. Bai, X. Kang, D. Liu, J. Gui, RSC Adv. 5 (2015) 42736–42743.
[49] S. Yan, Z. Li, Z. Zou, Langmuir 25 (2009) 10397–10401.
[50] Y. Liu, Z. Wang, B. Huang, K. Yang, X. Zhang, X. Qin, Y. Dai, Appl. Surf. Sci. 257 (2010) 172–175.
[51] Q. Lin, L. Li, S. Liang, M. Liu, J. Bi, L. Wu, Appl. Catal. B: Environ. 163 (2015) 135–142.
[52] F. Dong, A. Zheng, Y. Sun, M. Fu, B. Jiang, W.-K. Ho, S. Lee, Z. Wu, CrystEngComm 14 (2012) 3534–3544.
[53] J. Zhang, G. Zhang, X. Chen, S. Lin, L. Möhlmann, G. Dołęga, G. Lipner, M. Antonietti, S. Blechert, X. Wang, Angew. Chem. 124 (2012) 3237–3241.
[54] H. Huang, Y. He, X. Li, M. Li, C. Zeng, F. Dong, X. Du, T. Zhang, Y. Zhang, J. Mater. Chem. A 3 (2015) 24547–24556.
[55] S. Shamaila, A.K.L. Sajjad, F. Chen, J. Zhang, Appl. Catal. B: Environ. 94 (2010) 272–280.
[56] L. Chen, R. Huang, S.-F. Yin, S.-L. Luo, C.-T. Au, Chem. Eng. J. 193 (2012) 123–130.
[57] F. Dong, Y. Sun, W.-K. Ho, Z. Wu, Dalton Trans. 41 (2012) 8270–8284.
[58] B. Long, J. Lin, X. Wang, J. Mater. Chem. A 2 (2014) 2942–2951.
[59] K.S. Sing, Pure Appl. Chem. 57 (1985) 603–619.
[60] Y.-S. Xu, W.-D. Zhang, Appl. Catal. B: Environ. 140 (2013) 306–316.
[61] Y.J. Pagán-Torres, J.M.R. Gallo, D. Wang, H.N. Pham, J.A. Libera, C.L. Marshall, J.W. Elam, A.K. Datye, J.A. Dumesic, ACS Catal. 1 (2011) 1234–1245.
[62] S. Chen, Y. Hu, S. Meng, X. Fu, Appl. Catal. B: Environ. 150 (2014) 564–573.
[63] E. Goímez Alvarez, H. Wortham, R. Strekowski, C. Zetzsch, S. Gligorovski, Environ. Sci. Technol. 46 (2012) 1955–1963.
[64] J.-L. Shie, C.-H. Lee, C.-S. Chiou, C.-T. Chang, C.-C. Chang, C.-Y. Chang, J. Hazard. Mater. 155 (2008) 164–172.
[65] Z. Ai, W. Ho, S. Lee, L. Zhang, Environ. Sci. Technol. 43 (2009) 4143–4150.
[66] S. Ge, L. Zhang, Environ. Sci. Technol. 45 (2011) 3027–3033.
[67] J. Xu, Y. Wang, Y. Zhu, Langmuir 29 (2013) 10566–10572.